

Statistical analysis of Multi-Material Components using Dual Energy CT

Christoph Heinzl, Johann Kastner, Torsten Möller, and Eduard Gröller

Upper Austrian University of Applied Sciences, Wels Campus
GrUVi-Lab at Simon Fraser University

Vienna University of Technology, Institute of Computer Graphics and Algorithms

Email: {c.heinzl, j.kastner}@fh-wels.at,
torsten@cs.sfu.ca, groeller@cg.tuwien.ac.at

Abstract

This work describes a novel method for statistical analysis of multi-material components. The application scenario is industrial 3D X-ray computed tomography, emphasizing metrology of artefact affected plastics-metal components. The presented work makes use of dual energy CT data acquisition for artefact reduction, in order to optimize CT scans of multi-material components. Using statistical analysis, information on uncertainty is introduced, which allows detailed characterizations of single materials as well as material interfaces.

The major contribution of this paper is the development of a specific pipeline based on the dual exposure technique of dual energy CT. After prefiltering and multi-scan fusion, the statistical analysis step computes probability volumes of the fused data using a local histogram analysis technique. The application areas as well as the achieved precision of the presented method are depicted using a test specimen and a real world component.

1 Introduction

State-of-the-art engineering continuously rises the complexity of industrial components. To assure the quality of new components, also the demands in quality control are strongly increasing, requiring new, top of the line techniques. An upcoming means of quality assurance especially in the pre-production phase is industrial 3D X-ray computed tomography (3DCT). 3DCT is a non-touching and non-destructive method, which allows a fast characterization of a specimen. The main application areas of 3DCT are none destructive testing and metrology (the science of measurement), which the presented work is focussed on. Figure 1 shows a

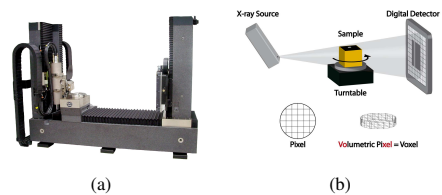


Figure 1: Photograph (a) and principle scheme (b) of an industrial 3D X-ray computed tomography system. General design: X-ray source (left), rotary plate (center), matrix detector (right). A single rotation is sufficient to fully characterize a specimen.

photograph of a dual source 3DCT device and the principle of 3DCT, which can be summed up as follows: At each angular position of a 360 degree turn of the specimen, a penetration image containing the X-ray attenuation is recorded. These penetration images are used to compute a 3D grid of greyvalues corresponding to the spatial X-ray attenuation [7]. 3DCT is the only method in metrology, which fully characterizes a specimen concerning outer, inner and even hidden structure of a specimen. Furthermore, 3DCT has the potential to overcome current limitations of conventional optical and tactile metrology, *e.g.*, reflecting or transparent probes, deformable probes, accessibility / visibility of the measured surface.

One of the most critical issues in the area of metrology using industrial 3DCT is the problem of artefacts. The characteristics and strength of an artefact is mainly determined by the specimen's geometry, the penetration lengths, the position and orientation in the cone beam, the measurement parameters and the specimen's material combination. Some of the most common artefact types are noise

induced streaks, beam hardening, partial volume, aliasing, and scattered radiation [7]. In the area of metrology artefacts may seriously affect or even prevent reliable metrology. Especially when scanning multi-material components severe streaking artefacts are introduced due to major changes in attenuation from one projection to the next. We addressed this problem in our previous work [6] reducing artefacts by data fusion of DECT scans.

A further critical problem is the lack of information on the uncertainty of an extracted surface, and in consequence, on the quality of the extracted dimensions. For surface extraction in industrial applications, usually a single isovalue is specified to distinguish between material and air. More recently, research activities concentrate on local surface extraction, *e.g.*, [2], [4] and [20]. Both local and global surface extractions consider the surface as ground truth for subsequent measurements. As each extracted surface only contains sharp borders characterizing the supposed boundary between materials, the entire information on the quality of the interface is lost.

This paper introduces a novel approach which addresses both the problem of artefacts and the problem of uncertainty. For artefact reduction of multi-material components, dual energy CT (DECT) is used. After prefiltering, a gradient magnitude based fusion step combines the two complementary DECT datasets, featuring the strength of each dataset. Using Bayesian classification, a probability volume is extracted containing the probabilities of each single material. Subsequent evaluations are based on the probability dataset.

2 Related Work

2.1 Dual Energy CT

Dual energy CT (DECT) was originally used for characterization of organic and inorganic materials in baggage control systems for airport security and for examination of drilling cores concerning material properties [8]. More recently the application area of DECT was expanded to medical and finally industrial CT. The main idea of DECT is to utilize different X-ray spectra in order to optimally characterize multi-material probes. DECT is facilitated by two different techniques: the dual exposure / dual source and the dual detector technique [14]. The

dual detector technique generates two datasets in one scan by using multi-layer-detectors, sensitive to different energy bands. 3DCTs with a single layer detector are limited to the dual exposure technique. The used 3DCT device is equipped with a single layer detector, featuring a high precision microfocus and a high power macrofocus X-ray source. Therefore the dual exposure technique is used in this approach.

2.2 Multi-Scan Fusion

In multi-scan fusion (MSF) recent advances either focus on enhancing projection images, respectively sinograms or on the reconstructed volumetric datasets. Sinograms are used by Oehler et al. [13] for artefact correction and are currently a topic of research for multi-scan fusion. As we do not have access to projection images respectively sinograms, these methods are out of scope.

A straight forward approach of MSF is dual viewing: Specimens are scanned twice at different positions and orientations [17] in the cone beam. Local data fusion allows to identify and reduce artefacts by considering the differences in gradient magnitude and greyvalue. However, orientation-invariant artefacts or artefacts affecting the same region can not be eliminated. More sophisticated approaches exploit DECT to combine multiple, corresponding slices images [17] or multiple volumetric datasets [6]. We apply a fusion scheme similar to Heinzl et. al [6], but instead of only fusing edge regions and neglecting material regions, we propose a multi-scan fusion scheme, which combines the complete datasets. The presented fusion scheme emphasizes the complementary strengths (the main object structure of the macrofocus scan and the crisp edges of the microfocus scan), avoiding irregularities in the histogram due to only considering edge regions.

2.3 Statistical Analysis

Recent advances in the area of statistical analysis focus on uncertainty visualization, fuzzy segmentation, and transfer function design. An overview of uncertainty visualization is outlined by the following techniques: Wittenbrink et al. [21] are using geometric glyphs visualizing uncertainty in vector field data. Kniss et al. [10] proposed a method

to explore uncertainty, risk, and probabilistic decision of surface boundaries in direct volume rendering (DVR). Rheingans and Joshi [15] proposed the rendering of the likelihood domain itself. Rhodes et al. [16] are mapping the confidence of isosurfaces to hue or texture. In this approach, we color-code uncertainty on isosurfaces and show a color-coded DVR of a probability datasets.

In fuzzy segmentation, each voxel has a degree of belonging to a region, facilitating segmentation at subvoxel accuracy. The importance of fuzzy classification with respect to material boundaries is discussed by Tzeng and Ma [19]. Grigoryan and Rheingans [5] employ a point cloud approach representing the spatial uncertainty in segmented data. Stalling et al. [18] use additional probability information in order to supplement region labels. In this work, we are using the spatial probabilities of each material to fuzzy segment a real world component.

In the area of transfer function design, Bajaj et al. [1] introduced the contour spectrum, which performs statistical analysis to create transfer function lookup tables. Multidimensional transfer functions, introduced by Levoy [11], enhance the transfer function domain using additional dimensions. While Levoy suggested the use of the gradient magnitude, Kindlmann et al. [9] even included the second derivative. Due to artefacts and overlapping regions, multidimensional transfer functions turned out to be unusable.

In the presented approach, we follow the idea of Kniss et al. [10] to use statistical classification for generating information on uncertainty of CT datasets. We introduce a pipeline model, which automatically classifies individual materials in an easy to use process. In particular, our approach is based on local histogram analysis using partial range histograms, which were originally introduced by Lundström et al. [12].

3 Pipeline for Statistical Analysis of Multi-Material Components

To facilitate statistical analysis of artefact affected industrial CT data, a customized pipeline was developed. The pipeline for statistical analysis of multi-material components is based on dual energy CT and combines prefiltering, multi-scan fusion and statistical analysis (Figure 2). The pipeline is demonstrated step by step on a real world compo-

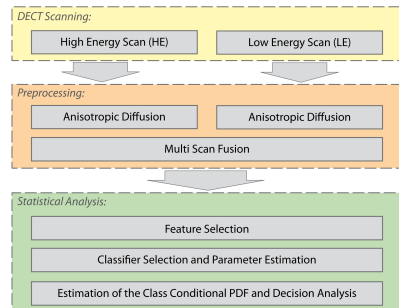


Figure 2: Principle scheme of the pipeline for statistical analysis of multi-material components. Input: HE and LE dataset, Output: probability volume.

nent, the Rubik’s Cube (for a detailed description of specimen one see section 4.1.1).

3.1 Dual Energy CT Scanning

DECT scans are facilitated by two subsequent scans without moving the specimen: A low energy (LE) microfocus scan yields a highly detailed but artefact affected scan. It generates better scanning results for low absorbing materials. However, severe artefacts are introduced in the presence of high absorbing components (see bright and dark streaks in Figure 3a). The subsequent high energy (HE) macrofocus scan yields maximal penetration lengths. HE scans generate almost artefact free results, but the bigger focal spot of the X-ray source introduces additional blur (Figure 3b).

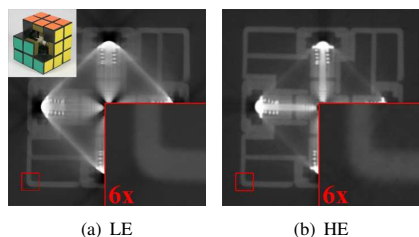


Figure 3: Specimen one: Axial cross sections through Rubik’s cube dataset. Severe artefacts modify greyvalues of LE scan (a) near high absorbing components. (b) Less artefact affected but more blurry HE scan (see magnified detail image, photograph courtesy of R. Frisch).

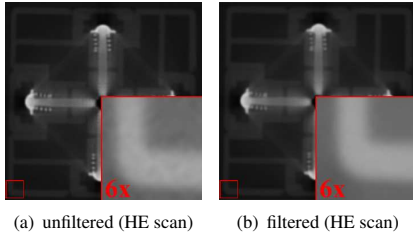


Figure 4: Axial cross sections through HE scan of specimen one before (a) and after (b) filtering. The dataset’s inherent noise is significantly reduced without moving or degrading edges. For a better visualization of the inherent noise, a contrast windowing was applied on the detail images.

3.2 Preprocessing

3.2.1 Anisotropic Diffusion Filtering

A preprocessing step is used to reduce the propagation of noise and smaller artefacts through the pipeline. For prefiltering without moving or degrading edges, the anisotropic diffusion filtering of HE and LE data is used similarly to our previous work [6] (see Figure 4).

3.2.2 Multi-Scan Fusion

To reduce artefacts, which especially emerge when scanning multi-material components, a custom fusion scheme was developed. The aim of this step is to extract details of the LE scan, without introducing artefacts. Compared to our previous work [6], a smooth fusion throughout the whole dataset has to be ensured to prevent modifications of the sta-

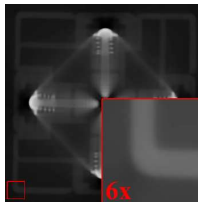


Figure 5: Axial cross section through fused dataset of specimen one. Compared to LE scan, artefacts are significantly reduced. The detail image shows a smooth characteristic of the greyvalues with sharp edges.

tistical greyvalue distribution, which is undesirable in statistical analysis. In the first step the region type (RT) of each voxel is determined using spatial greyvalues and gradient magnitudes. Three different region types are distinguished: homogeneous, transition, and artefact affected region. At each spatial position the weights for LE and HE dataset are computed according to the region type. In artefact affected regions, only the HE dataset is considered and weighted with 1. Homogeneous regions are equally weighted for noise reduction. For transition regions a Sigmoid function is used in the range of 0.5 to 1.0, weighting the greyvalues of each dataset according to the local gradient magnitude of the preprocessed HE scan. Compared to a linear

Algorithm 1 Multi Scan Fusion (MSF)

Δ_{GV} (greyvalue (GV) difference HE-LE dataset);
 Δ_{GM} (gradient magnitude (GM) difference HE-LE);
 ϵ_{GV} (max GV difference); ϵ_{GM} (max GM difference); c_{min} (min GM); c_{GM} (GM transition)

```

procedure MSF( $\epsilon_{GV}, \epsilon_{GM}, c_{min}, c_{GM}$ )
  for all corresponding voxels  $\in LE, HE$  do
     $RT \leftarrow RegionType(\epsilon_{GV}, \epsilon_{GM}, c_{min}, c_{GM})$ 
    if  $RT == ArtefactAffected$  then
       $w_{LE} \leftarrow 0; w_{HE} \leftarrow 1$ 
    else if  $RT == Transition$  then
       $w_{LE} \leftarrow Sigmoid(GM_{HE} - c_{GM})$ 
       $w_{HE} \leftarrow (1 - w_{LE})$ 
    else
       $w_{LE} \leftarrow 0.5; w_{HE} \leftarrow 0.5$ 
    end if
     $Fused \leftarrow (w_{LE} * GV_{LE} + w_{HE} * GV_{HE})$ 
  end for
end procedure

```

```

procedure REGIONTYPE( $\epsilon_{GV}, \epsilon_{GM}, c_{min}, c_{GM}$ )
  if ( $|\Delta_{GV}| > \epsilon_{GV}$  or  $|\Delta_{GM}| > \epsilon_{GM}$ ) then
     $RT \leftarrow ArtefactAffected$ 
  else
    if ( $\Delta_{GM} > c_{min}$  &  $GM_{HE} > c_{GM}$  &  $GM_{LE} > c_{GM}$ ) then
       $RT \leftarrow Transition$ 
    else
       $RT \leftarrow Homogeneous$ 
    end if
  end if
  return  $RT$ 
end procedure

```

weighting, the Sigmoid function allows a stronger consideration of the detailed LE scan to achieve sharper boundaries (see Algorithm 1 and Figure 5).

3.3 Statistical Analysis

For statistical analysis, Bayes' decision theorem is applied. The basis of Bayesian decision theory is the idea of quantifying trade-offs and costs in classification decisions. Classifications using Bayesian decision theory consists of 3 major steps: 1) feature selection, 2) selection and estimation of the classifier, and 3) estimation of the class conditional PDF and decision analysis. Bayes' decision theorem provides the relationship between class conditional and posterior probability. The class conditional probability is defined as the probability of an event A, given the occurrence of an other event B. The posterior probability of a random event is the conditional probability that is assigned after the relevant evidence is taken into account.

3.3.1 Feature Selection

In the case of statistical analysis of multi-material components the task of the classifier is to distinguish between the different materials. Firstly, each material is assigned to a class ω_j , *e.g.*, plastic-metal components: $\omega_0 \leftarrow \text{air}$, $\omega_1 \leftarrow \text{plastics}$ and $\omega_2 \leftarrow \text{metal}$. The second task is to select "good" features to distinguish the different classes. A "good" feature is discriminating, easy to extract and should be position, orientation and scale invariant. For decomposing CT datasets into single materials, the spatial greyvalues are used as feature. Including more dimensions to the feature vector, *e.g.*, gradient magnitude or 2nd derivative, does not necessarily result in a better classifier. Due to artefacts and performance issues of the classification, the feature vector was not extended.

3.3.2 Classifier Selection and Parameter Estimation

The selection of a reliable classifier is the most critical step. To construct the classifier, the following assumptions are applied for 3DCT: Homogeneous materials should generate constant greyvalues. Due to partial volume effects, greyvalues are modified in edge regions of a material. Furthermore, irregularities are introduced due to the characteristics of

detector and X-ray source as well as the 3D reconstruction. As the greyvalues of a homogeneous material tend to be continuously distributed, the classifier is modelled by a probabilistic distribution (probability density function $p(\mathbf{x}|\omega_j)$, \mathbf{x} denotes a sample feature vector). Based on these assumptions we consider the classifier to be Gaussian-distributed for the subsequent steps.

Gaussian curve fitting is used to setup the probability density function (PDF) $p(\mathbf{x}|\omega_j)$ of a class ω_j . An expectation maximization scheme based on Gaussian mixture models, which was applied to the global histogram, turned out to produce suboptimal PDFs. Due to the overlapping characteristic of the material distributions in the histogram, especially of the low absorbing material and air, the Gaussian parameters degenerated.

In contrast, local histogram analysis allows to reconstruct each material's histogram H_{ω_j} . We apply a method for histogram decomposition, which is based on Lundström et al. [12]. Initially, the histogram of a dataset is divided into partial range histograms (PRH). PRHs are regional sub-histograms around a local maximum in the range of $\mu \pm \alpha * \sigma$ (α denotes range of considered standard deviations). In order to reconstruct each material's histogram H_{ω_j} by recombination of PRHs, Lundström et al. rely on a custom heuristic for medical datasets, which is not applicable to uncalibrated industrial CT data. Therefore we developed a new recombination method, which is based on weighted multi-dimensional KMeans and applicable on datasets of any domain: For each extracted PRH a feature vector is defined, which consists of μ and σ . While μ corresponds to the highest peak in the PRH, σ is estimated by Gaussian curve fitting, minimizing the accumulated height difference. The wider the partial ranges $\mu \pm \alpha * \sigma$, the more data of the PRH is considered for the fit. As in each PRH only one feature is dominant, α of 2 covers the range of about 95% of the Gaussian distribution for the fit.

For recombination of the PRHs to a material's histogram H_{ω_j} , weighted KMeans [3] is used. The extracted feature vector of each PRH is weighted with the sum of frequencies in the PRH. This allows preferring larger PRHs over smaller ones. KMeans clustering requires the number of clusters to be separated, which corresponds to the number of defined classes ω_j . Using random initial cluster centers,

KMeans assigns each feature vector to the nearest center, with respect to the Euclidean distance. After the feature vectors are classified, a new cluster center is calculated and the algorithm restarts. If the cluster centers are not changing anymore, the final cluster centers are found. Finally the PRHs of each cluster are combined to generate each material's histogram H_{ω_j} .

To estimate the classifier for a class ω_j , the parameters of the PDF $p(\mathbf{x}|\omega_j)$ of each material's histogram H_{ω_j} have to be estimated. μ_{ω_j} is considered to coincide with the highest peak in the histogram. To reduce errors of irregularities and smaller spikes in the histogram, σ_{ω_j} is calculated as the mean of two estimations: Firstly, $\sigma_{\omega_j,1}$ is estimated by a Gaussian curve fitted to the peak of the material's sub-histogram with a wide partial range using $\alpha = 2$. Secondly, the overall standard deviation $\sigma_{\omega_j,2}$ of the histogram H_{ω_j} is calculated. A mean of both estimations $\sigma_{\omega_j,1}$ and $\sigma_{\omega_j,2}$ guarantees a robust probability density function $p(\mathbf{x}|\omega_j)$. The resulting material histograms for each class ω_j of specimen one and the corresponding PDFs $p(\mathbf{x}|\omega_j)$ are depicted in Figure 6.

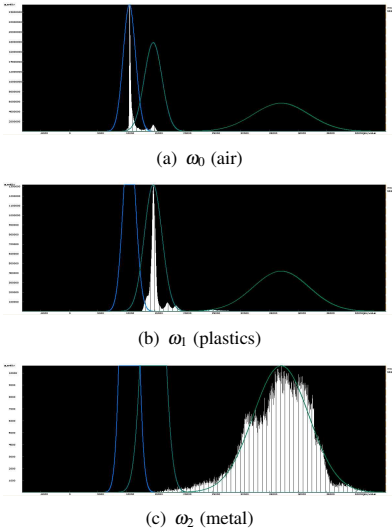


Figure 6: Resulting histograms of specimen one for class ω_0 (air) (a), ω_1 (plastics) (b) and ω_2 (metal) (c). The blue to green graphs depict the extracted PDFs $p(\mathbf{x}|\omega_j)$ scaled to the maximum of the corresponding histogram peak.

3.3.3 Estimation of Class Conditional PDF and Decision Analysis

For decision analysis a probability dataset is calculated from the prefiltered and fused LE and HE datasets. The probability dataset contains a probability vector at each spatial position. The scalar values of a probability vector contain the posterior probabilities of the corresponding spatial greyvalue of belonging to a considered class ω_j . The probability vector is calculated using Bayes' theorem:

$$p(\omega_j|\mathbf{x}) = \frac{p(\mathbf{x}|\omega_j)P(\omega_j)}{p(\mathbf{x})}, \quad (1)$$

The posterior $p(\omega_j|\mathbf{x})$ of a random event weights the class conditional PDF $p(\mathbf{x}|\omega_j)$ against the observed evidence $p(\mathbf{x})$ and the prior information $P(\omega_j)$. Class conditional PDFs $p(\mathbf{x}|\omega_j)$ describe the probabilities of a greyvalue belonging to a certain class ω_j . The evidence is defined as

$$p(\mathbf{x}) = \sum_{j=1}^c p(\mathbf{x}|\omega_j)P(\omega_j), \quad (2)$$

which is the sum of all class conditional PDFs $p(\mathbf{x}|\omega_j)$. The evidence serves as a scaling factor, which guarantees the posterior probabilities $p(\omega_j|\mathbf{x})$ to sum to 1. The prior probability value $P(\omega_j)$ is a marginal probability, which describes the statistical probability of a material ω_j when picking a random position in the dataset.

In order to calculate the probability volume of a fused DECT dataset, first of all the prior probabilities $P(\omega_j)$ for each material have to be determined. As the volumetric ratios of a material should not influence local boundaries, the priors $P(\omega_j)$ for each material ω_j are evenly set to $1/(j+1)$. The class conditional PDF $p(\mathbf{x}|\omega_j)$ is estimated using the local histogram approach introduced in subsection 3.3.2. The evidence $p(\mathbf{x})$ is calculated using equation 2 and the posterior $p(\omega_j|\mathbf{x})$ using equation 1. In Figure 7 the resulting posterior probability volume of specimen one is depicted. Figure 7a shows an axial cross section which depicts the posterior probability of class ω_0 (air), Figure 7b of class ω_1 (plastics) and Figure 7c of class ω_2 (metal). Bright areas depict regions with high probabilities, dark regions vice versa. In this context probability volumes allow robust and reproducible fuzzy segmentations of each material.

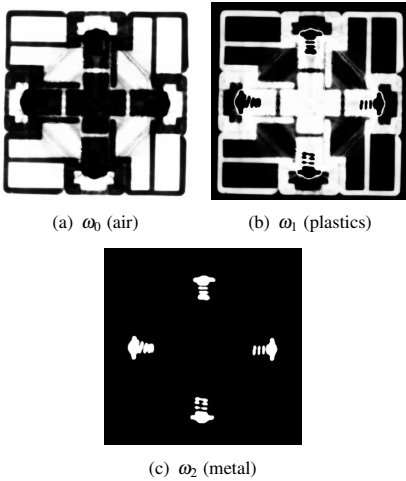


Figure 7: Axial cross section through resulting probability volume of specimen one depicting the probabilities of air (a), plastics (b) and metal (c) and the implicit fuzzy segmentation of each material. Bright regions refer to high probabilities, dark regions to low ones. Minor modifications due to HE dataset are still visible in probability volume.

4 Results and discussion

All evaluated specimens are multi-material components consisting of low absorbing material (plastics) and high absorbing material (metal). The CT scans were performed on a HWM RayScan 250E system with a 225 kV microfocus and a 450 kV macrofocus X-ray source. The measurement parameters are listed in Table 1. As reference, CAD models are used. The demo application was implemented in Visual C++ using ITK and VTK.

Table 1: Measurement Parameters

Parameter	$Spec1_{HE}$	$Spec1_{LE}$	$Spec2_{HE}$	$Spec2_{LE}$
projections	810	810	900	900
U (kV)	420	150	440	200
I (μ A)	1200	400	1300	450
t_{int} (ms)	285	500	2000	1000
filter plates	1mm W 1.5mm Cu	1mm Cu	1mm W 1.5mm Cu	1mm Cu
extent[X]	401	401	508	508
extent[Y]	401	401	523	523
extent[Z]	401	401	611	611
voxelsize (μ m)	200	200	200	200

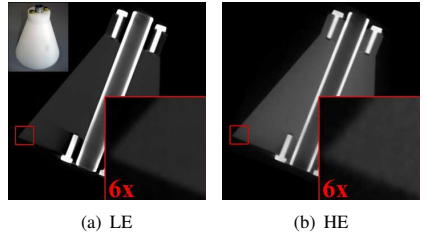


Figure 8: Specimen two: Axial cross sections through TP03 dataset. LE scan (a) shows severe artefacts in presence of metallic screws. Compared to LE, the HE scan (b) is less artefact affected but less precise and contains more noise (see magnified detail image).

4.1 Specimens

4.1.1 Specimen one: Rubik's Cube

Specimen one (Figure 3) is a mechanical puzzle. The original Rubik's cube consists of 3 intermediate levels in height, width and depth. Each face is covered by nine stickers of one of six solid colors. Disassembling the cube returns 21 pieces: a core piece consisting of three intersecting axes, which hold the six center squares, and twenty smaller plastic pieces for the subsections. The six squares of the core piece are mounted to the axis cross using six steel screws. Springs pushing the squares of the core piece allow flexible movement of the axes.

4.1.2 Specimen two: TP03

Specimen two (Figure 8) is a polyethylene (PE) test-part consisting of a cone with an attached cylinder. Six smaller drill holes are placed on the top, at the bottom and on the shell of the component. The central drill and the six smaller drill holes are equipped with screws and a steel bar, in order to artificially create a multi-material component.

4.2 Tuning the pipeline

The differentiation between the different region types in the fusion step is controlled by greyvalue and gradient magnitude based parameters. The parameters ϵ_{GM} , ϵ_{GV} and c_{GM} are determined by histogram analysis of difference datasets, which contain the spatial differences in greyvalue respectively

gradient magnitude. ϵ_{GM} and ϵ_{GV} are used to specify the main peak range of the corresponding histogram, while c_{GM} sets the minimum between the transition air to low absorbing material. c_{min} is a negative value depicting the minimal threshold of ΔGM , which helps to avoid streaking artefacts in the fused result. It is supposed to be lower than ϵ_{GM} and set in the range of $0.5 * \epsilon_{GM}$ to ϵ_{GM} . The extraction of partial range histograms requires two parameters to control the extraction process of each material’s histogram. ϵ_{PRH} controls the generation and extent of PRHs. The higher ϵ_{PRH} , the more homogeneous is the corresponding region of a PRH, but also the more PRHs are extracted. Values between 0.8 and 0.9 proved to be a good trade-off between number of extracted PRHs and homogeneity. Furthermore, the precision of a PRH is controlled by the neighborhood size N . 8^3 is a typical setting for our datasets. To capture more filigree structures lowering the size N is suggested. Due to the weighted multi-dimensional KMeans PRH recombination, the specification of further parameters is not necessary.

4.3 Evaluation of results

4.3.1 Extraction of PDFs

The extraction of class conditional PDFs and the corresponding posteriors is demonstrated using specimen two. Narrow PDFs $p(\mathbf{x}|\omega_j)$ result in sharp transitions of the posterior $p(\omega_j|\mathbf{x})$. However, sharp transitions generate segmentation-like probability volumes, which degenerate the extracted probability surfaces to jagged representations. Wide and overlapping probability density functions allow the calculation of posteriors with

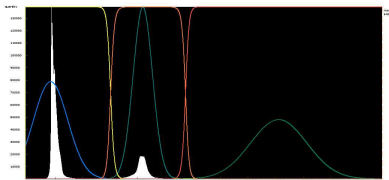


Figure 9: Histogram of specimen two. Blue to green graphs depict the extracted class conditional PDFs $p(\mathbf{x}|\omega_j)$ of each material. Yellow to orange graphs plot smooth and overlapping posteriors $p(\omega_j|\mathbf{x})$ for calculating the probability volume.

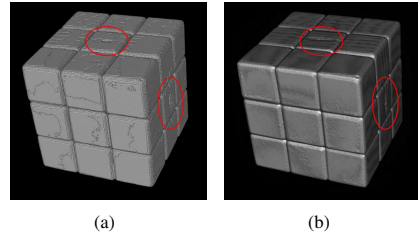


Figure 10: Volume rendering of threshold-based binary segmentation (a) and fuzzy segmentation (b) of plastics of specimen one. Fuzzy segmentation generates a precise representation of the segmented material (see red circles).

smooth transitions, which serve for calculating probability volumes with fuzzy transitions. Figure 9 depicts the extracted class conditional PDFs $p(\mathbf{x}|\omega_j)$ (blue to green graphs) and the resulting posteriors $p(\omega_j|\mathbf{x})$ (yellow to orange graphs) in the corresponding histogram.

4.3.2 Fuzzy segmentation

Another application area realized by probability volumes is fuzzy segmentation. Common segmentation methods based on binary encoding are lacking information on uncertainty. Probability volumes contain spatial probability values and therefore an implicit fuzzy segmentation. Using fuzzy segmentation, transition and artefact affected regions are considered with decreased probability values and do not generate jagged structures due to binary segmentation. Figure 7 depicts axial cross sections of each material of specimen one. Figure 10 shows volume renderings of a threshold based binary segmentation (a) and the resulting fuzzy segmentation (b) of the plastics class of the Rubik’s cube dataset.

4.3.3 Metrology

To get an overview of a surface model’s deviations compared to reference geometry data, actual/nominal comparisons are widely used. Actual/nominal comparisons color-code deviations between the surfaces of test model and reference model on the surface of the reference model. Figure 11 depicts 4 actual/nominal comparisons (reference: CAD model): The upper 2 images depict

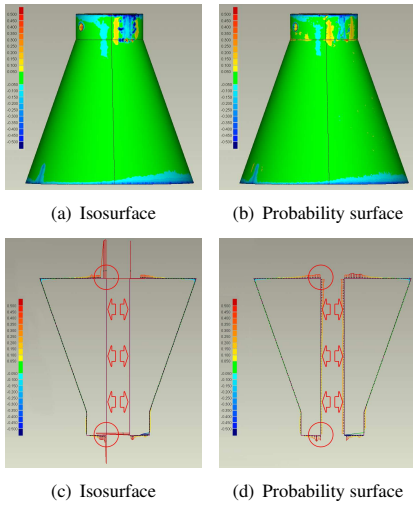


Figure 11: Actual/nominal comparisons of probability surface and isosurface of specimen two. Outer surface shows similar deviations. 2D cross sections reveal that only the probability approach captures internal transitions (red circles and arrows).

3D actual/nominal comparisons of the best global isosurface (a) respectively isoprobability surface (b). Compared to the isosurface, the actual/nominal comparison of the isoprobability surface shows similar or marginally lower deviations on the outer surface. To reveal internal deviations, two 2D comparisons are carried out on the best global isosurface (c) respectively isoprobability surface (d). A 2D actual/nominal comparison shows the deviations of reference and test model on the contour of the reference's surface at a predefined cutting plane. 2D actual/nominal comparisons reveal the major advantage when using probability volumes on internal structures. The global isosurface is not able to capture transitions to neighboring higher absorbing material and lower absorbing material using one single threshold (c). Erroneous results are generated due to incomplete data (red circles). The isoprobability surface facilitates an evaluation of all transitions to all neighboring materials (d).

4.3.4 Uncertainty Visualization

Visualizing uncertainty allows an overall estimation on the quality of a scan. We present two different approaches, uncertainty mapping and direct vol-

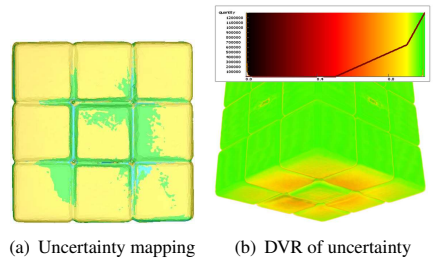


Figure 12: Uncertainty visualization. Color coding of an isosurface of specimen one mapping interpolated uncertainty on the surface (a). DVR using color and opacity transfer functions (b). Bottom area with elevated uncertainty due to greyvalue modifications caused by the specimen holder.

ume rendering of probability data demonstrated on the Rubik's cube: Using uncertainty mapping (Figure 12a), the interpolated spatial uncertainty values of a considered class are color-coded on the evaluated surface. Blue regions depict high uncertainty, while yellow indicates low uncertainty. The green areas depict elevated uncertainty due to minor deformations and smaller artefacts (scattered radiation between the subsections of each level in the cube). Figure 12b shows a direct volume rendering (DVR), color-coding the probabilities using a color and opacity transfer function. Green depicts high probabilities of 95 - 100%, while red depicts probabilities down to 50%. Elevated uncertainty is clearly visible in the bottom section due to greyvalue modifications caused by the specimen holder.

5 Conclusion

A novel pipeline for statistical analysis of multi-material components is presented applying DECT for artefact reduction. After prefiltering and multi scan fusion, the statistical analysis is carried out by computing probability volumes using a local histogram analysis technique. The accuracy and the applicability of the pipeline has been discussed using a test part and a real world component. The wide-spread application areas can be found in fuzzy segmentations, metrology applications and uncertainty visualization. In our future work we will further increase the precision of the pipeline and explore additional uncertainty visualizations.

Acknowledgements

The presented work has been funded by the FH-Plus project ZfP of the Austrian Research Promotion Agency (FFG) and partly supported by the PVG project, Austrian Science Fund (FWF) grant no P18547.

References

- [1] C. L. Bajaj, V. Pascucci, and D. R. Schikore. The contour spectrum. In *IEEE Visualization 1997*, pages 167–173, 1997.
- [2] S. Bischoff and L. Kobbelt. Isosurface reconstruction with topology control. In *Pacific Conference on Computer Graphics and Applications*, pages 246–255, 2002.
- [3] R. O. Duda, P. E. Hart, and D. G. Stork. *Pattern Classification (2nd Edition)*. Wiley-Interscience, 2000.
- [4] S. F. F. Gibson. Constrained elastic surface nets: generating smooth surfaces from binary segmented data. In *MICCAI 1998*, pages 888–898, 1998.
- [5] G. Grigoryan and P. Rheingans. Point-based probabilistic surfaces to show surface uncertainty. In *IEEE TVCG*, volume 10, pages 564–573, 2004.
- [6] C. Heinzl, J. Kastner, and E. Gröller. Surface extraction from multi-material components for metrology using dual energy CT. In *IEEE TVCG*, volume 13, pages 1520–1527, 2007.
- [7] J. Hsieh. *Computed Tomography: Principles, Design, Artifacts and Recent Advances*. SPIE-The International Society for Optical Engineering, 2003.
- [8] M. Iovea, O. Dului, G. Oaie, C. Ricman, and G. Mateiasi. Dual-energy computer tomography and digital radiography investigation of organic and inorganic materials. In *European Conference on Non Destructive Testing*, 2006.
- [9] G. Kindlmann and J. W. Durkin. Semi-automatic generation of transfer functions for direct volume rendering. In *IEEE Symposium on Volume Visualization*, pages 79–86, 1998.
- [10] J. Kniss, R. V. Uitert, A. Stephens, G. Li, and T. Tasdizen. Statistically quantitative volume visualization. In *IEEE Visualization 2005*, pages 287–294, 2005.
- [11] M. Levoy. Display of surfaces from volume data. In *IEEE Computer Graphics and Applications*, volume 8, pages 29–37, 1988.
- [12] C. Lundström, P. Ljung, and A. Ynnerman. Local histograms for design of transfer functions in direct volume rendering. In *IEEE TVCG*, volume 12, pages 1570–1579, 2006.
- [13] M. Oehler and T. M. Buzug. A sinogram-based metal artifact suppression strategy for transmission computed tomography. In *Geometriebestimmung mit industrieller Computertomographie, PTB-Bericht PTB-F-54*, pages 255–262, Braunschweig, 2007.
- [14] V. Rebuffel and J.-M. Dinten. Dual-energy x-ray imaging: benefits and limits. In *European Conference on Non Destructive Testing*, 2006.
- [15] P. Rheingans and S. Joshi. Visualization of molecules with positional uncertainty. In E. Gröller, H. Löffelmann, and W. Ribarsky, editors, *Data Visualization '99*, pages 299–306. Springer-Verlag Wien, 1999.
- [16] P. J. Rhodes, R. S. Laramée, R. D. Bergeron, and T. M. Sparr. Uncertainty visualization methods in isosurface rendering. In M. Chover, H. Hagen, and D. Tost, editors, *Eurographics 2003*, pages 83–88, 2003.
- [17] R. Schmitt, P. Hafner, and S. Pollmanns. Kompensation von Metallartefakten in tomographischen Aufnahmen mittels Bilddatenfusion. In *Proceedings of Industrielle Computertomographie, Fachtagung 2008*, pages 117–122, 2008.
- [18] D. Stalling, M. Zökler, and H. Hege. Interactive segmentation of 3D medical images with subvoxel accuracy. In H. Lemke, K. Inamura, M. Vannier, and A. Farman, editors, *Computer Assisted Radiology and Surgery*, pages 137–142, 1998.
- [19] F.-Y. Tzeng and K.-L. Ma. A cluster-space visual interface for arbitrary dimensional classification of volume data. In *IEEE/EG Symposium on Visualization*, pages 17–24, 2004.
- [20] R. T. Whitaker and D. E. Breen. Level-set models for the deformation of solid objects. In *3rd international workshop on implicit surfaces*, pages 19–35, 1998.
- [21] C. M. Wittenbrink, A. T. Pang, and S. K. Lodha. Glyphs for visualizing uncertainty in vector fields. In *IEEE TVCG*, volume 2, pages 266–279, 1996.